Space-Time Dense Multipath Components Modeling at mmWaves in Indoor Industrial Environments

Frederic Munoz*†, Gloria Makhoul*†, Davy P. Gaillot §, Claude Oestges‡ Raffaele D'Errico*†
*Cea-Leti, Grenoble, France, emails: frederic.munoz@cea.fr, gloria.makhoul@cea.fr, raffaele.derrico@cea.fr
†University of Grenoble-Alpes, Grenoble, France
‡ICTEAM, Université catholique de Louvain, Louvain-La-Neuve, Belgium
§University of Lille, CNRS, UMR 8520 - IEMN Lille, davy.gaillot@univ-lille.fr

***Abstract*—This paper presents the characterization and models of specular and dense multipath components in the millimeter wave channels for industrial scenarios. The results are obtained from measurements covering the 26 - 30 GHz bands and employing a massive virtual array. Two different high-resolution algorithms, SAGE and RiMAX, have been employed. Then, a beamforming on the dense component is performed to obtain their angular distribution. The results are compared in terms of large-scale parameter fitting.**

***Index Terms*—Indoor Factory channel, millimeter-waves propagation, dense multipath component.**

I. Introduction

The massive multiple-input multiple-output (mMIMO) and millimeter wave (mmW) are key technologies to meet 6G network requirements in data-rates, enhanced coverage, and reduced latency [1]. The numerical transformation of the manufacturing process in industrial environments is expected to enable wireless data transfer between machine at high data rates, monitoring and localization of unmanned vehicle position inside the industrial environment and automation of the entire production cycle. Nevertheless, accessing these technologies goes with better accuracy in the propagation channel models for any industrial scenarios. In this case, the difficulty arises from the highly reflective environment that produces a more complex electromagnetic scenario, thus leading to a challenging study of the propagation model.

In the literature, multi-band measurements at 6.75 GHz and 30 GHz were presented in [2] considering line-of-sight (LOS) and non-LOS (NLOS) propagation. Another comparative study of channel characteristics, i.e. path loss and Ricean K-factor, was presented in [3], in the frequency bands of 4.9 and 28 GHz. The result analysis indicated that severe attenuation and lower multipath richness occur at 28 GHz. In [4], [5], large-scale parameters were characterized based on measurements at 28 GHz in LOS and NLOS scenarios. The Power Delay Profiles (PDPs) were also evaluated showing that the channel contains Dense Multipath Components (DMCs). Recently, the 3rd Generation Partnership Project (3GPP) released a first 5 G IIoT standard model, regarding PL, LOS probability, delay and angular spreads, taking into account clutter density and antenna height, for frequency ranges from 0.5 GHz to 100 GHz [6]. However the DMCs have not been addressed in the model and left for further investigation.

Conventional high-resolution algorithms such as SAGE allows for an estimation of the Specular Multi-path Components (SMCs), corresponding to the dominant concentrated propagation paths from a ray-based model, but it does not estimate the DMCs, caused by the distributed diffuse scattering, spatial or temporal distribution. Nonetheless, DMCs can have a major impact in communication system performance, especially in NLOS scenarios where the DMCs power contribution to the propagation channel is large [7]. In a previous analysis of the measurements used in this paper [8], it was shown that the DMCs power ratio is around 40 % - 60 % and the contribution of the DMCs in the NLOS case was larger compared to the LOS case as expected. An accurate modeling of the DMCs can also improve the localization accuracy [9] even allowing to determine the position of a user without any estimated SMCs [10].

In this paper, the DMCs parameters are analyzed and its effects on the propagation model parameter estimation are characterized from the measurements carried out in indoor factory [8]. The SAGE SMCs estimated from the previous study [8] are compared with the newly generated RiMAX SMCs. Note that RiMAX provides a DMC distribution with the joint estimation of the SMCs and DMCs. This distribution is only in the temporal domain as described in [11]. To further highlight the interest in the DMCs modeling, the SAGE and RiMAX SMCs parameters and overall DMCs power ratio will be compared between them. Moreover, large-scale parameters are estimated in order to see how the proposed methodologies compare with the propagation channel measurements.

This paper is structured as follows. Section II presents the measurement campaign. Section III is dedicated to the SAGE - RiMAX SMCs parameters estimation and DMCs power ratio. Section IV describes the beamforming process and the DMCs distribution space-time modeling. Finally, Section V compares the large-scale parameters obtained from the various methods to the measured ones.

II. Measurement campaign

The measurement campaign investigated in this study is the same as in [8]. A visualisation of the industrial-like environment can be seen in Fig. 1. It is an Indoor Factory (InF) environment. The propagation channel is measured with a $5 \times 5 \times 5$ with 5 mm inter-space cubic virtual array at the

Fig. 1: Image of the measurement environment in a LOS scenario.

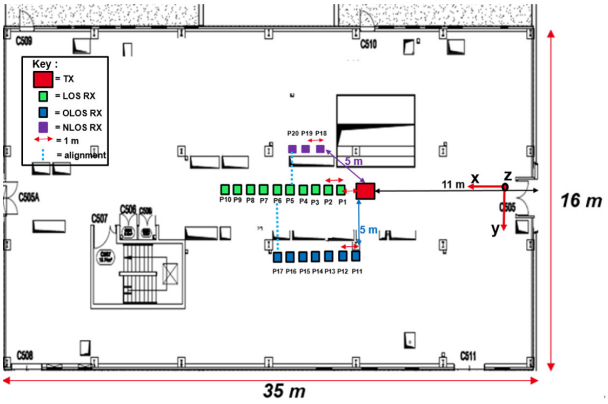

Fig. 2: Measurement setup presenting the LOS, OLOS and NLOS scenarios.

transmitter (Tx) side using a vertically polarized monopole antenna. At the receiver (Rx) side, another vertically polarized monopole antenna is placed at 20 positions inside the room. Depending on Rx position with respect to Tx position, LOS, OLOS or NLOS conditions were measured. The propagation channel was sounded with a VNA from 26 GHz to 30 GHz with a 5 MHz sampling frequency. The transmitted power was set to 10 dBm at Tx with a 100 Hz Intermediate Frequency Band Width (IFBW) . A 20 dB LNA was used at the Rx side for dynamic purposes.

Fig. 2 describes the floor plan. The room dimensions are 35 m $\times$ 16 m $\times$ 3.5 m. The roof is mostly metallic whereas the floor is made out of concrete. The ventilation duct, metal beam and cabinets around the Rx and Tx antennas are highly reflective.

For each Rx position, the Tx virtual cubic array acquisition is performed by an automated setup between the VNA and the x-y-z positioning system.

III. Channel parameter estimation

The SMCs are estimated using the SAGE [12] and RiMAX [13] high-resolution algorithms. This section presents the approaches used to estimate the characteristics of the DMCs in the two algorithms and compares the results for SMCs and DMCs obtained with both algorithms.

A. RiMAX

For the RiMAX implementation, a temporal power distribution of one DMC is estimated. The DMC is assumed to be Kronecker-separable in the spatial and frequency domains with a spatially white distribution in the angular domain [11]. Therefore, the estimated DMC Power Delay Profile (PDP) has an exponential decaying power profile such as:

$$\psi(\tau) = \begin{cases} 0, & \tau < \tau_d \\ \alpha_d/2, & \tau = \tau_d \\ \alpha_d e^{-B_d(\tau-\tau_d)}, & \tau > \tau_d \end{cases}, \quad (1)$$

where α_d is the DMC peak power, B_d is the decay factor and τ_d is the base delay. Additionally, a white Gaussian noise with power α_0 is assumed to be included in the measurement.

In order to select the most significant path, five new SMCs are created at each iteration of the RiMAX algorithm. The Signal to Noise Ratio (SNR) of each estimated SMC is compared with a threshold. This threshold corresponds to the probability that the SMC belongs to the noise. Since the RiMAX algorithm provides an estimate of the Fisher information matrix, the SMC variance is readily obtained by the diagonal coefficient of the inverse Fisher information matrix [11]. Therefore, to be considered as a reliable SMC, the following criterion has to be respected for the SMC complex amplitude estimation $\widehat{\alpha}_l$:

$$SNR(\widehat{\alpha}_l) = \frac{|\widehat{\alpha}_l|^2}{\mathrm{var}\left(|\widehat{\alpha}_l|\right)} \geq 4.32\,dB \quad (2)$$

In other words, each SMC exceeding a 4.32 dB SNR has a 90 % probability of being a reliable SMC and not belonging to the noise process. The algorithm stops when all new estimated SMCs fail this criterion. An overall DMC power ratio is readily obtained from the DMC PDP and the measured PDP.

B. SAGE

With SAGE, once the algorithm stops estimating new SMCs following a given criterion, it is possible to deduce the overall DMCs power ratio with the following equation [8]:

$$DMCs(\%) = \frac{\sum_{f=f_{\min}}^{f_{\max}} |H_{meas}(f) - H_{SAGE}(f)|^2}{\sum_{f=f_{\min}}^{f_{\max}} |H_{meas}(f)|^2} \times 100. \quad (3)$$

In contrast to RiMAX, the stopping criterion for the SAGE algorithm is a given threshold in dB which depends on the estimated noise floor power of the measurement.

C. SMCs & overall DMCs power ratio comparison

For the Rx position P5, a comparison of the Average Power Delay Profile (APDP) and SMCs , in powers represented relatively by the size of their markers, as well as the Angle of Departure (AOD) in Azimuth/Elevation estimated with SAGE and RiMAX are presented in Fig. 3 and Fig. 4, respectively.

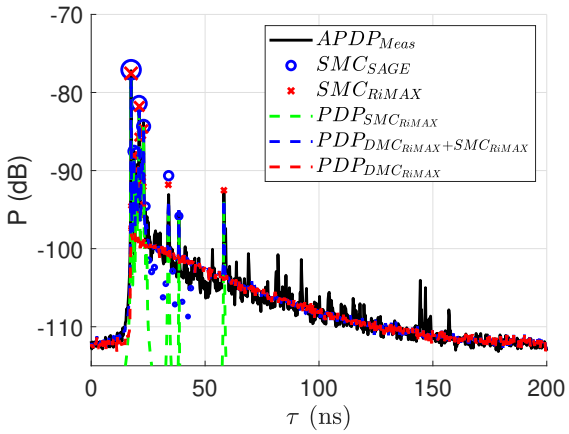

Fig. 3: Average Power Delay Profile (APDP) at P5 with RiMAX/SAGE estimates.

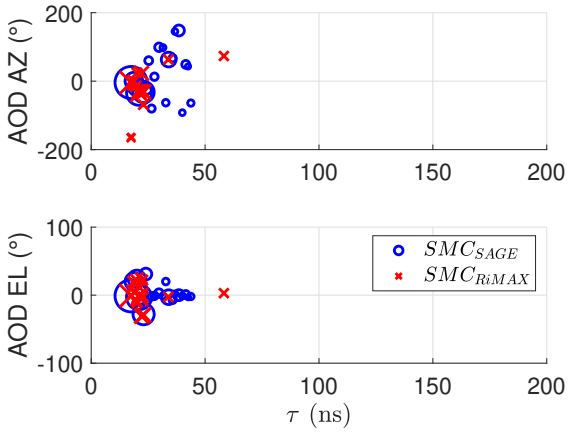

Fig. 4: Comparison at P5 between RiMAX and SAGE for angle of departure (AOD) in azimuth (AZ) and elevation (EL) planes.

It is observed that the strongest SMCs are coherent except for the weakest SMCs estimated by SAGE. Indeed, the stopping criterion differs between the two techniques such that RiMAX filters out any SMCs below the estimated DMC.

Fig. 5 describes the evolution of the overall DMC power ratio with the receiver position. For the three scenarios, the number of estimated SMCs by RiMAX is lower than the one estimated by SAGE. Again, this number mostly depends on the SMC selection threshold used in each algorithm. This is particularly true for the OLOS and NLOS cases. This results in a 10 % to 30 % additional overall DMC power ratio with RiMAX. As a matter of fact, this effect is attributed to weak SMCs that belong to the DMC. Alternatively, this yields an under evaluation of the DMC power ratio percentage with SAGE.

IV. DMCs SPATIO-TEMPORAL MODELING

In order to develop further a DMCs spatio-temporal modeling and more specifically to obtain the DMCs spatial distribution, a conventional Bartlett beamformer was applied on the 125 measurements given by the Tx virtual array. For each array element i, the SAGE reconstructed frequency response is subtracted from the measurement. Then, the Bartlett beamformer [14] is applied on the virtual cubic array with the SAGE estimated $H_{i,DMC}$ at each frequency. As seen in Fig. 4, the SMCs are mostly distributed in the azimuth plane. Hence, the beamforming is performed in this plane.

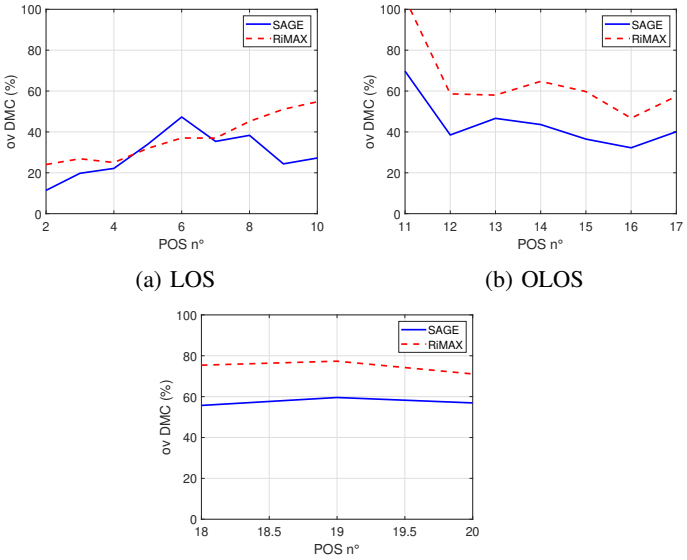

(a) LOS (b) OLOS

(c) NLOS

Fig. 5: InF overall DMC power ratio over position.

Cluster boundaries in azimuth can be used to fit a spatio-temporal distribution of DMC associated to one SMC cluster [15]. This DMC represents the diffuse part of the cluster not detected in the SMCs estimation. A K-means algorithm is applied to the SAGE SMCs to arrange the SMCs into clusters. For each cluster k, the cluster mean value and standard deviation are obtained for the delay ($\tau^{k,cluster}$, $\sigma_{\tau}^{k,cluster}$) and azimuth dimension ($\phi^{k,cluster}$, $\sigma_{\phi}^{k,cluster}$). The cluster azimuth boundaries are defined by its mean value and Azimuth Angular Spread (AAS). Then, a Von-Mises Distribution (VMD) is adjusted with a maximum likelihood estimator between the cluster boundaries for each delay. The VMD parameters of each cluster k are then obtained from the delay mean value and are characterized by a mean location value μ_{ϕ}^{k} and a concentration parameter value κ_{ϕ}^{k}.

Fig. 6 shows the resulting response obtained from the beamformer h_{DMC} as well as one VMD fit inside the cluster boundaries ($k = 2$ here).

To obtain the DMCs delay distribution, the Power Azimuth Delay Profile (PADP) obtained from the inverse Fourier transform of H_{DMC} is integrated over the k^{th} cluster azimuth boundaries:

$$\psi_{DMC}^{(k)}(\tau) = \frac{1}{4\pi^2} \int_{\phi_{\min,k}}^{\phi_{\max,k}} |h_{DMC}(\phi, \tau)|^2 d\phi, \qquad (4)$$

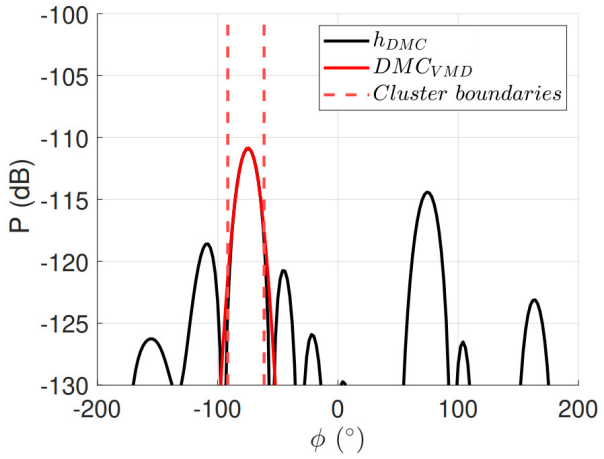

Fig. 6: PADP DMC azimuth distribution at $\tau = 25\ ns$ for P5 with DMC model associated to the SMCs cluster $k = 2$.

where $\phi_{\max,k} = \phi^{k,cluster} + \sqrt{2}\sigma_\phi^{k,cluster}$ and $\phi_{\min,k} = \phi^{k,cluster} - \sqrt{2}\sigma_\phi^{k,cluster}$.

The parameter vector $\zeta^{(\mathbf{k})} = [\alpha_d^{(k)}, B_d^{(k)}, \tau_d^{(k)}]$ describing the exponential decaying profile (see (1)) for the k^{th} cluster associated DMC is estimated following [16]:

$$\widehat{\zeta^{(k)}} = \arg\min_{\zeta^{(k)}} \sum_{m=0}^{M-1} \left| \psi_{DMC}^{(k)}(\tau_m) - \psi^{(k)}(\tau_m, \zeta^{(k)}) \right|^2. \quad (5)$$

From the knowledge of the DMCs space-time distribution, it is possible to visually show how the PADP from the modeled distributions compares with the estimated PADP DMCs.

For the Rx position P5, Fig. 7 and Fig. 8 present the mean value in the delay and azimuth domains of the five found clusters, respectively. The modeled DMCs are well centered to the clusters centroid in the angular domain. In contrast, the DMC base delay τ_d does not necessarily follow the mean delay of its associated cluster. Therefore, the spatial correlation between clusters and DMCs makes sense in our scenarios while the DMCs distribution in the delay space looks decoupled from the clusters temporal structure.

TABLE I: DMC and Cluster relation

DMC Parameter	Cluster Parameter Value
$\mu_\phi^k(^\circ)$	$0.99 \cdot \phi^{k,cluster}$
$1/\kappa_\phi^k$	$2.45 \cdot 10^{-6} \cdot (\sigma_\phi^{k,cluster}(^\circ))^2 + 0.02$
$\alpha_d^k(dB)$	$0.35 \cdot P^{k,cluster}(dB) - 136.25$
$B_d^k(dB/\mu s)$	$4.7 \cdot 10^{-3} \sigma_\tau^{k,cluster}(ns) + 15.6$
$\tau_d^k(ns)$	$0.105 \cdot \tau^{k,cluster}(ns) + 15.18$

To illustrate how the DMCs relate to the SMCs clusters parameters, the following Table I is given.

In Table I, it can be seen that the DMCs parameters μ_{phi}^k and $1/\kappa_\phi^k$ are related to the clusters mean azimuth value and the cluster variance in azimuth, respectively.

The peak power DMCs α_d^k are related to the cluster mean power, but the slope and base delay DMCs are less related to the cluster delay spread and mean delay than it was reported by [15]. For instance, this weak relation of the DMCs base delay to the clusters mean delay can directly be seen in Fig. 8.

V. Large-scale parameters comparison

To investigate how the additional information obtained from the estimated DMCs distribution improves the channel estimation, the Delay Spread (DS) and Azimuth Angular Spread (AAS) for the LOS, OLOS ans NLOS scenarios are computed for each position as follows:

$$DS = \sqrt{\frac{\sum_{l=1}^{L}(\tau_l - \mu_{\tau_l})^2 \alpha_l^2}{\sum_{l=1}^{L} \alpha_l^2}} \quad (6)$$

$$AAS = \sqrt{-2ln\left(\left|\frac{\sum_{l=1}^{L} e^{j\phi_l}\alpha_l^2}{\sum_{l=1}^{L} \alpha_l^2}\right|\right)}, \quad (7)$$

where μ_{τ_l} is the mean delay.

Finally, the mean value and standard deviation for the DS and AAS obtained from the measurement are compared to

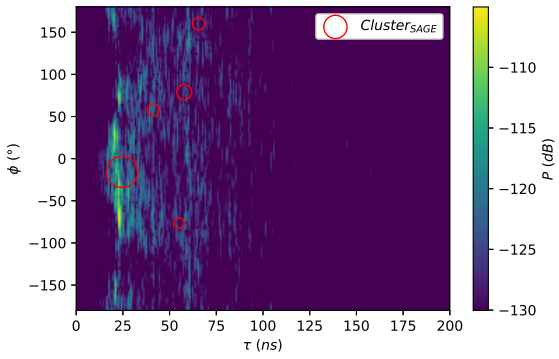

Fig. 7: Estimated DMCs PADP and SMCs cluster mean values LOS.

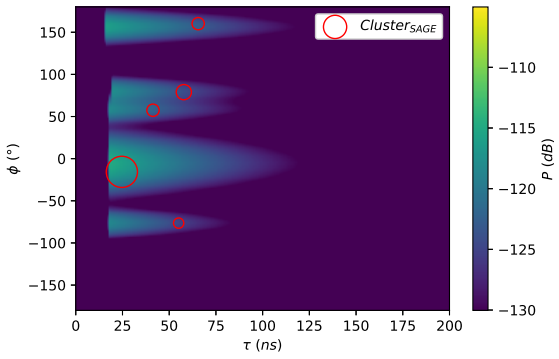

Fig. 8: Modeled DMCs PADP and SMCs cluster mean values LOS.

TABLE II: Scenarios InF

LOS	μ_{DS} (ns)	$10^{\sigma_{lgDS}}$	μ_{AAS} $(^\circ)$	$10^{\sigma_{lgAAS}}$
Measurement	15.92	1.52	42	1.20
RiMAX	12.13	1.87	39	2.35
SAGE	7.78	1.84	22	1.87
SAGE + DMCs	18.32	1.57	43	1.40
3GPP	21.67	1.41	36	1.78
OLOS + NLOS	μ_{DS} (ns)	$10^{\sigma_{lgDS}}$	μ_{AAS} $(^\circ)$	$10^{\sigma_{lgAAS}}$
Measurement	24.83	1.26	71	1.48
RiMAX	16.18	2.56	51	2.11
SAGE	15.73	1.69	39	1.79
SAGE + DMCs	23.72	1.21	65	1.47
3GPP	26.07	1.55	37	1.58

those obtained with the SAGE, RiMAX, SAGE + DMCs and 3GPP channel model parameters [6]. The results presented in Table II are obtained by averaging the values of each position for the LOS, OLOS and NLOS scenarios. Table I shows how the large scale parameters depend on the propagation condition. The following observations can be drawn:

- The measured μ_{DS} is lower than the 3GPP model in the LOS scenario. Inversely μ_{AAS} is higher in measurement than with the model. Meanwhile for OLOS+NLOS scenario μ_{DS} measured is in good agreement with the 3GPP InF NLOS model but the μ_{AAS} measured is much higher, 71 , than the 3GPP value 37 .
- The comparison between the RiMAX and SAGE estimated parameter shows how the joint estimation of the DMC delay distribution improves the estimated DS and AAS compared to the measured value.
- Finally, the SAGE + DMCs methodology gives a close estimate to the measurement for the angular large-scale parameter, both in terms of mean value and standard deviation. As for the temporal dimension, RiMAX shows good performance in the LOS scenario, the SAGE + space-time distributed DMCs only provides better estimate in DS for the OLOS+NLOS scenario.

VI. Conclusion

In this paper, the mmW radio channel in an indoor industrial environment was studied under LOS, OLOS and NLOS scenarios through two high-resolution algorithms, SAGE and RiMAX. First, the SMCs estimated from both techniques were analyzed. Then, with a clustering algorithm applied on the SAGE SMCs, the DMCs spatio-temporal distribution estimation was carried out after spatial filtering around the clusters angular distribution. It was shown that the DMCs spatial distribution is well correlated with the clusters angular parameters whereas the temporal distribution does not show such a high correlation value between them. The DMCs space-time distribution estimation relevance was illustrated by computing the DS and AAS mean and standard deviation for the three shadowing scenarios. Indeed, the SAGE estimated SMCs, with the addition of the DMCs, give the closest large-scale parameter estimated to the one measured. This demonstrates the interest into evaluating the channel dense part distribution in indoor industrial environments, not only in the delay domain but also in the angular domain.

Acknowledgment

This work has been funded by the French National Agency for Research (ANR) under the project named S2LAM and the French government under the Recovery Plan (CRIIOT project)

References

[1] M. A. Uusitalo, P. Rugeland, M. R. Boldi, E. C. Strinati, P. Demestichas, M. Ericson, G. P. Fettweis, M. C. Filippou, A. Gati, M.-H. Hamon, M. Hoffmann, M. Latva-Aho, A. Pärssinen, B. Richerzhagen, H. Schotten, T. Svensson, G. Wikström, H. Wymeersch, V. Ziegler, and Y. Zou, "6g vision, value, use cases and technologies from european 6g flagship project hexa-x," *IEEE Access*, vol. 9, pp. 160 004–160 020, 2021.

[2] D. Dupleich, R. Muller, M. Landmann, J. Luo, G. D. Galdo, and T. R. S., "Multi-band characterization of propagation in industry scenarios," in *2020 14th European Conference on Antennas and Propagation (EuCAP)*, 2020, pp. 1–5.

[3] Y. Guan, J. Zhang, L. Tian, P. Tang, and T. Jiang, "A comparative study for indoor factory environments at 4.9 and 28 ghz," in *2020 14th European Conference on Antennas and Propagation (EuCAP)*, 2020, pp. 1–5.

[4] M. Schmieder, F. Undi, M. Peter, E. Koenig, and W. Keusgen, "Directional wideband channel measurements at 28 ghz in an industrial environment," in *2019 IEEE Global Communications Conference (GLOBECOM)*, 2019, pp. 1–6.

[5] M. Schmieder, T. Eichler, S. Wittig, M. Peter, and W. Keusgen, "Measurement and characterization of an indoor industrial environment at 3.7 and 28 ghz," in *2020 14th European Conference on Antennas and Propagation (EuCAP)*, 2020, pp. 1–5.

[6] T. Jiang, J. Zhang, P. Tang, L. Tian, Y. Zheng, J. Dou, H. Asplund, L. Raschkowski, R. D'Errico, and T. Jamsa, "3gpp standardized 5g channel model for iiot scenarios: A survey," *IEEE Internet of Things Journal*, vol. 8, no. 11, pp. 8799–8815, 2021.

[7] A. Richter, J. Salmi, and V. Koivunen, "Distributed scattering in radio channels and its contribution to mimo channel capacity," in *2006 First European Conference on Antennas and Propagation*, 2006, pp. 1–7.

[8] A. Mudonhi, G. Makhoul, M. Lotti, R. D'Errico, and C. Oestges, "Mmwave massive mimo channel sounding in industrial iot scenarios," in *2022 Joint European Conference on Networks and Communications 6G Summit (EuCNC/6G Summit)*, 2022, pp. 53–58.

[9] F. Wen, J. Kulmer, K. Witrisal, and H. Wymeersch, "5g positioning and mapping with diffuse multipath," *IEEE Transactions on Wireless Communications*, vol. 20, no. 2, pp. 1164–1174, 2021.

[10] Y. Ge, F. Wen, H. Kim, M. Zhu, F. Jiang, S. Kim, L. Svensson, and H. Wymeersch, "5g slam using the clustering and assignment approach with diffuse multipath," *Sensors*, vol. 20, no. 16, p. 4656, 2020.

[11] E. Tanghe, D. P. Gaillot, M. Liénard, L. Martens, and W. Joseph, "Experimental analysis of dense multipath components in an industrial environment," *IEEE Transactions on Antennas and Propagation*, vol. 62, no. 7, pp. 3797–3805, 2014.

[12] B. Fleury, M. Tschudin, R. Heddergott, D. Dahlhaus, and K. Ingeman Pedersen, "Channel parameter estimation in mobile radio environments using the sage algorithm," *IEEE Journal on Selected Areas in Communications*, vol. 17, no. 3, pp. 434–450, 1999.

[13] A. Richter, "Estimation of radio channel parameters: Models and algorithms." ISLE Blacksburg, VA, USA, 2005.

[14] B. D. Van Veen and K. M. Buckley, "Beamforming: A versatile approach to spatial filtering," *IEEE assp magazine*, vol. 5, no. 2, pp. 4–24, 1988.

[15] F. Quitin, C. Oestges, F. Horlin, and P. De Doncker, "Diffuse multipath component characterization for indoor mimo channels," in *Proceedings of the Fourth European Conference on Antennas and Propagation*. IEEE, 2010, pp. 1–5.

[16] N. Czink, A. Richter, E. Bonek, J.-P. Nuutinen, and J. Ylitalo, "Including diffuse multipath parameters in mimo channel models," in *2007 IEEE 66th Vehicular Technology Conference*. IEEE, 2007, pp. 874–878.